Title

Evolution of the Valley Position in Bulk Transition-Metal Chalcogenides and Their Monolayer Limit

Journal

Nano Letters, 16(8)

ISSN

1530-6984

Authors

Yuan, Hongtao

Liu, Zhongkai

Xu, Gang

et al.

Publication Date

2016-08-10

DOI

10.1021/acs.nanolett.5b05107

Peer reviewed

Evolution of the Valley Position in Bulk Transition-Metal Chalcogenides and their Mono-Layer Limit

Hongtao Yuan[1,2], Zhongkai Liu[1,2,3,4], Gang Xu[1], Bo Zhou[5,6], Sanfeng Wu[7], Dumitru Dumcenco[8,9], Kai Yan[1,2], Yi Zhang[6], Sung-Kwan Mo[6], Pavel Dudin[10], Victor Kandyba[11], Mikhail Yablonskikh[11], Alexei Barinov[11], Zhixun Shen[1,2], Shoucheng Zhang[1,2], Yingsheng Huang[8], Xiaodong Xu[7], Zahid Hussain[6], Harold Y. Hwang[1,2*], Yi Cui[1,2,12*], and Yulin Chen[3,4,5,10*]

[1]*Geballe Laboratory for Advanced Materials, Stanford University, Stanford, California 94305, USA*

[2]*Stanford Institute for Materials and Energy Sciences, SLAC National Accelerator Laboratory, Menlo Park, California 94025, USA*

[3]*School of Physical Science and Technology, ShanghaiTech University, Shanghai 200031, China*

[4]*CAS-Shanghai Science Research Center, 239 Zhang Heng Road, Shanghai 201203, China*

[5]*Physics Department, Clarendon Laboratory, University of Oxford, Parks Road, Oxford, OX1 3PU, UK*

[6]*Advanced Light Source, Lawrence Berkeley National Laboratory, Berkeley, California 94720, USA*

[7]*Department of Physics, Department of Materials Science and Engineering, University of Washington, Seattle, Washington 98195, USA*

[8]*Department of Electronic and Computer Engineering, National Taiwan University of Science and Technology, Taipei, Taiwan (ROC)*

[9]*Electrical Engineering Institute, Ecole Polytechnique Federale de Lausanne (EPFL), CH-1015 Lausanne, Switzerland*

[10]*Diamond Light Source, Didcot, Oxfordshire, UK*

[11]*Elettra-Sincrotrone Trieste ScPA, Trieste, Basovizza 34149, Italy*

[12]*Department of Materials Science and Engineering, Stanford University, Stanford, California 94305, USA*

* *Correspondence should be addressed to:* hyhwang@stanford.edu, yicui@stanford.edu, Yulin.Chen@physics.ox.ac.uk

ABSTRACT:

Valley physics based on layered transition metal chalcogenides have recently sparked much interest due to their potential spintronics and valleytronics applications. However, most current understanding of the electronic structure near band valleys in momentum space is based on either theoretical investigations or optical measurements, leaving the detailed band structure elusive. For example, the exact position of the conduction band valley of bulk MoS_2 remains controversial. Here, using angle-resolved photoemission spectroscopy with sub-micron spatial resolution (micro-ARPES), we systematically imaged the conduction/valence band structure evolution across representative chalcogenides MoS_2, WS_2 and WSe_2, as well as the thickness dependent electronic structure from bulk to the monolayer limit. These results establish a solid basis to understand the underlying valley physics of these materials, and also provide a link between chalcogenide electronic band structure and their physical properties for potential valleytronics applications.

Keywords: Angle-Resolved Photoemission Spectroscopy, Band Structure, Transition Metal Dichalcogenides, Valleytronics

Recent efforts on graphene-like layered materials with novel properties have attracted much attention not only for potential electronic and spintronic devices[1, 2, 3, 4, 5, 6, 7, 8], but also more generally for energy storage[9] and catalytic applications.[10, 11] With a layered honeycomb lattice, transition metal dichalcogenides MX_2 (M = Mo, W; X = S, Se, Te) have two inequivalent valleys in the ***k***-space electronic structure in the hexagonal Brillouin zone (BZ).[12, 13, 14] Due to the large separation of valleys in ***k***-space and the resulting suppression of intervalley scattering, the valley index can be used in analogy to the spin in spintronics, opening a new research direction called 'valleytronics'.[12,14,15] Moreover, having heavy 4*d*/5*d* elements with strong spin-orbital interaction (SOI)[12, 16, 17], the monolayer MX_2 compounds show polarized spin texture in the electronic structure, as demonstrated theoretically[8, 18, 19] and supported by optical investigations[5, 7, 20], and thus are promising candidates for a new type of valley-coupled spintronics applications.[4, 5, 20, 21] However, despite these exciting developments, the detailed electronic structure of MX_2 compounds, especially the valley loci and their evolution, remain elusive. Different theories propose the location of the conduction band valley to be either at high-symmetry K points, the corner of the BZ, or at non-symmetric points along Γ-K direction.[16, 18, 22, 23, 24]

In this work, we directly studied the electronic structure of representative transition metal chalcogenides MoS_2, WS_2 and WSe_2 by high resolution ARPES, and observed the valley evolution in the band structure between different compounds. We found that although the valence band maximum (VBM, hole valley) of bulk MX_2 compounds always resides at Γ, the conduction band minimum (CBM, electron valley) loci shift from K (MoS_2) towards Γ (WS_2 and WSe_2). Moreover, by utilizing the novel spatially resolved ARPES technique (with 800nm spatial resolution) recently developed, we studied MoS_2 and WSe_2 micro-flakes with different thickness and observed the evolution of the electronic band structure and the band gap geometry from the bulk to the mono-layer limit. Our observations provide a solid understanding on the underlying valley physics of MX_2 materials and guidance for the design and the development of novel electronic/spintronics/valleytronics devices.

Typical valence and conduction band structures in bulk MoS_2. The crystal structure of 2H-MX_2 chalcogenides (Fig. 1a, with D_{6h}^4 symmetry and the $P6_3/mmc$ space group) comprises of stacked …X-M-X… triple-layer groups bonded by van der Waals force (Fig. 1a; we use "mono-layer" to refer to one such triple-layer unit), with the adjacent mono-layers rotated by 180° with respect to each other. The 3D BZ of MX_2 is illustrated in Fig. 1b with high symmetry points indicated. Due to the lack of inversion symmetry in each mono-layer, a net in-plane electric dipole moment is present at the M-atoms, which induces out-of-plane spin polarization near the valleys at K points via spin-orbit interaction (SOI).[8,21] Remarkably, as two adjacent mono-layers restore inversion symmetry by A-B stacking order (Fig. 1a), the band structure of such bi-layer MX_2 flakes remains spin-degenerate. As a result, the band structure of MX_2 chalcogenides can change dramatically from bi- to mono-layer and leads to valley locus evolution due to the change of interlayer coupling, for example the indirect-direct band gap transition.[22, 23, 25]

Figures 1c-g show the overall electronic structure of bulk MoS_2, the most broadly studied MX_2 compound.[2] Evidently, the VBM valley of MoS_2 clearly resides at the Γ point (Figs. 1c, e, f) and is ~0.5 eV above the top of the valence band at the K point. From Γ to K, the valence band evolves into two sub-bands with ~180 meV splitting (at K points, see Fig. 1c) caused by the strong SOI, in good agreement with previous theoretical calculations,[22, 23, 25] ARPES measurements[26,27] and our *ab initio* calculations (see Fig. S1 in the supplementary information, SI). This splitting in the band structure at the K points also results in two triangular pockets in the constant energy contours (e. g. at -0.8 eV, see Fig. 1d, e). The difference between the valence band-top at K and Γ points is as large as 0.5 eV. In addition to the k_x-k_y dispersions, we also investigate the k_z-dispersion of the band structure of MoS_2 with the photon energy dependent ARPES study (the details can be found in the SI, part II and Fig. S2), which indicates that the bands around Γ disperse dramatically along k_z, while those around K do not. This two-dimensional behavior of the bands around K supports the band

calculations indicating their origin as the localized in-plane Mo-$d_{x^2-y^2}$ and Mo-d_{xy} orbitals, while the three dimensional behavior of the bands around Γ originate from the delocalized out-of-plane *Mo*-$d_{3z^2-r^2}$ and *S*-p_z orbitals.[26] This observation clearly suggests that both decreasing sample thickness and changing elements in the compounds would tune the out-of-plane orbitals, change the bands around Γ and play a critical role in changing the valley positions in the band structure.

Since the Fermi energy (E_F) of as-grown MoS_2 samples is pinned inside the band gap close to the CBM by impurity states, we cannot directly observe the conduction band (Fig. 1c-e). In order to investigate the conduction band, we performed *in situ* electron doping by introducing a small amount of potassium onto the sample surface[27] (with K coverage as low as 0.0003 layer; details can be found in SI part II) and shift E_F. Note that the band structure of MoS_2 should not have any modification with such a small amount of dopant coverage. Using this method, we successfully lifted E_F into the conduction band [Fig. 1f, g and Fig. 2a-d (i)] and clearly observed that the CBM valleys of bulk MoS_2 are located at the K point – which differs from most current band calculations[16, 22, 23, 24] that suggest the CBM is located at some non-symmetric point (here denoted as Λ) along the Γ– K direction. From Fig. 1f, the indirect band gap of MoS_2 is found to be ~1.4 eV and the VBM valley of MoS_2 resides at Γ (Fig. 1d and f) and is ~0.5 eV above the apex of the valance band at the K point. From our measurement, the effective mass of the hole pockets is ~0.8 m_0 for the VBM at Γ and ~0.5 m_0 for the VBM at K, also consistent with our *ab initio* calculations (more details of the effective mass can be found in Part I of SI) and other recent ARPES reports[25, 26, 27].

Determination of CBM/VBM valley positions in bulk MX_2. In contrast to the small SOI in the MoS_2, W-based MX_2 compounds such as WS_2 and WSe_2 have a larger SOI strength, which will potentially result in large spin splitting with the broken inversion symmetry. Therefore we performed further ARPES measurements on WS_2 and WSe_2. As illustrated in Fig. 2a(i-iii), with the increase of atomic mass from Mo to W and from S to Se, the splitting of the VBM valleys at the K points

increases (MoS_2: ~180 meV, WS_2: ~470 meV and WSe_2: ~500 meV) due to the increased atomic SOI. An interesting observation is that although the VBM valley still resides at Γ for all three materials, the difference between peaks of the valence band at Γ and K dramatically decreases from 0.5 eV [MoS_2, Fig. 1f and Fig. 2a(i)] to 0.05 eV [WSe_2, Fig. 2a(iii)]. The fact that the valence band maxima of WSe_2 at Γ and K are very close to each other may have important implications for hole-type spin based device applications[19, 28], such as recent demonstration of electrical control of spin polarization and spin transport by tuning E_F to the vicinity of the apexes at the K points[8].

To compare the CBM positions of the three compounds, we again performed *in situ* K-doping on the sample surface (Fig. 2b-d). As expected, all three compounds show an indirect band gap (Fig. 2b,c). Remarkably, although the bulk band gap remains indirect for all three compounds, the CBM location evolves from the K point (MoS_2) to the Λ point (WSe_2), as is evident in both the band dispersions (Fig. 2c) and the Fermi surface (FS) maps (Fig. 2d) – a direct experimental observation that pins down the exact CBM position and the size of the direct/indirect band gap in different MX_2 compounds. This finding not only clarifies the controversy on the CBM loci,[16, 22, 23, 24] but also provides critical information for designing function devices with MX_2 materials (e.g. in "valleytronics", the operation depends on the band minima/maxima positions).

***Ab initio* calculations for CBM/VBM valley positions.** To understand the discrepancy between previous theoretical reports[16, 22, 23, 24], we performed systematic *ab initio* studies on the band structure of these materials, which demonstrated that the crystal structural parameters (e.g. in-plane lattice parameter *a* and out-of-plane parameter *d* of MX_2, see Fig. 1a and discussed below) can have strong influence on the band structure. These results are summarized in Fig. 3 with more discussion in the SI. For example, as can be seen in Fig. 3a-c, the local valley locus of MoS_2 at Λ point moves up (with respect to that at K) with either increasing *a* or decreasing *d*; and one can see that changing the *a* (or *d*) value by only ±2.5% will dramatically change the band structure and the relative position of the valley loci at Γ and K. This effect can be summarized in Fig. 3d, where the 2D phase diagram

shows the energy difference between the conduction band minima at Λ and K ($\Delta E_{\Lambda K}^{CB} = \Delta E_{\Lambda}^{CB} - \Delta E_{K}^{CB}$) as a function of parameters *a* and *d*. Importantly, our calculation results using relaxed lattice parameter (red dot in Fig. 3d) indeed shows a positive $\Delta E_{\Lambda K}^{CB}$ (i.e. the CBM located at K rather than Λ), in agreement with the ARPES observation (Fig. 1f). Such strong dependence of the band structure on lattice parameters indicates that strain engineering could be an effective method to modulate the electronic structure of MX_2 materials in practical applications (e.g. induced indirect-direct band-gap transition by external strain).

To understand why the conduction band valley loci change with lattice parameters, we need to know the orbital components for the energy bands at K and Λ points. Note that the band valleys at K and Λ points originate from two different sub-bands with different orbital components: the subband near K points mainly consists of Mo-$d_{3z^2-r^2}$ along the out of plane direction, while the subband near the Λ point mainly comes from Mo-$d_{x^2-y^2}$ and Mo-d_{xy} orbitals which are confined in the 2D (x-y) plane, far away from the ligand S/Se atoms. So we can see that the valley position at Λ point has almost no change in the energy scale with the lattice constant. However, for the $d_{3z^2-r^2}$ orbital, since its lobes point to the ligand S/Se atoms, the minimum at K point becomes very sensitive to the distance to the ligand atoms. The overlap of the $d_{3z^2-r^2}$ orbital decreases with increasing *a*, lowering the energy level of the valleys at the K points (Fig. 3a). On the other hand, when *d* increases, the overlap of the d_{z^2} orbital also increases, lifting up the energy level of the valleys at the K points. Therefore the increase of *a* and *d* have opposite effects on the valley loci evolution (directly reflected by $\Delta E_{\Lambda K}^{CB}$ and $\Delta E_{\Gamma K}^{VB} = E_{\Gamma}^{VB} - E_{K}^{VB}$).

Interestingly, these two opposite effects from *a* and *d* have nearly the same influence (in both

cases, $\Delta E_{\Lambda K}^{CB}$ linearly shifts around 0.9 eV when the parameter changes ~5% in total, see Fig. 3c). This helps to explain the valley loci evolution from MoS_2, WS_2 to WSe_2: Compared to MoS_2, the parameter *a* for WSe_2 increases ~ 4.2%, while the distance *d* of WSe_2 is enlarged more than 7%. Since the changing of *d* is greater than *a*, it dominates the evolution of the valley locus. As we have observed in Fig. 2, the $\Delta E_{\Lambda K}^{CB}$ becomes negative, and the Λ point becomes the CBM valley in WSe_2, which is quite different from the case of MoS_2. In addition, we calculated a hypothetical system with *a* and *d* both enlarged by 4.2%. Very similar to MoS_2 itself, the CBM valley of the hypothetical system still sits at the K point, which further confirms the picture that the band valleys at K and Λ points originate from sub-bands with different orbital components.

Evolution of valley positions from bulk, bilayer to monolayer MX_2. Many of the potential applications of these materials are based on few-layers devices. Therefore, it is of great importance to investigate the valley evolution in the electronic structure of MX_2 materials with thickness down, ideally, to the mono-layer limit. For the layer-dependent band structure study, we mechanically exfoliated bulk samples (the same samples used for the ARPES study in Figs. 1, 2) and acquired bi- and mono-layer flakes. As the lateral size of these flakes is typically only several micrometers (as shown in Fig. 4b-d), which is much smaller than the photon beam used in typical ARPES, we adopted the recently developed spatially resolved (spatial resolution ~800 nm) ARPES technique for our study - which allowed the measurement of the band structure of sub-micron samples[25, 26] (the schematic of the instrument we used and the measurement geometry is depicted in Fig. 4a; more details can be found in SI part III). Interestingly, the same flakes used in the spatially-resolved ARPES measurements can also be directly used for other measurements (e.g. optics and transport) and device fabrication - thus establishing a direct link between the band structure and their important physical properties. Compared to the molecular beam epitaxy and chemical vapor deposition methods that have been used to obtain single layer MX_2 films, the exfoliation method not only is

much simpler, but also provides the opportunity to study the band structure of layered materials with different thicknesses in the same flake.

Figures 4b-d show the optical micrograph and atomic force microscopy (AFM) images of a typical exfoliated MoS_2 ultrathin flake used in our spatially-resolved ARPES study. Similar to graphene[29, 30, 31, 32, 33], one can determine the thickness of the flakes by their reflective colors, which is further confirmed by AFM (Fig. 4d) and spatially resolved Raman spectroscopy (Fig. 4e) on a MoS_2 flake[34]. As illustrated in Fig. 4d, the atomically flat surfaces of different thicknesses can typically span a few microns laterally, which is sufficiently large given our sub-micrometer spatial resolution. To illustrate the unique properties of monolayer MX_2, photoluminescence spectroscopy (Fig. 4f) was also performed at room temperature with excitation energy of 2.33 eV, yielding pronounced exciton emission from MoS_2 and WSe_2 monolayer while much suppressed in bulk[7, 20, 21].

In Fig. 5, we summarize the spatially-resolved ARPES results on the same flake used for the study in Fig. 4e. We were able to scan across the substrate and find the same flake by acquiring a photoemission intensity map [Fig. 5a (i~iii), with different magnification levels]. Comparing these maps to the optical image [Fig. 5a (iv)], we could easily identify the flake areas with different thicknesses, and three points (P1~P3) with mono-, bi- and multi-layers were chosen in our investigation. The band structures measured at points P1-P3 are illustrated in Figs. 5b and c, where Fig. 5b shows the maps of the constant energy contours at 0.5 eV binding energy; Fig. 5c gives the band dispersion along Γ-K and Γ-M high-symmetry directions. Indeed, a sudden switch of the VBM valley from K to Γ occurs when the thickness of the flake increases from mono- (spot P1) to bi-layer (spot P2) - which can be seen both in Fig. 5b [where the constant energy surface spots (valley loci) in panels (i) and (iii) are located at the K and Γ points, respectively] and Fig. 5c [where the VBM valleys of panels (i) and (iii) are located at the K and Γ points, respectively]. In contrast to this valley shift between mono- to bi-layer flakes, the band structure of bi-layer (spot P2) and multi-layers (spot P3) are quite similar and both have the valley sitting at the center of the BZ. This observation

unambiguously demonstrates that the interlayer interaction plays a critical role in the band structure evolution, and also the position of the VBM valleys changes from the Γ to K point with decreasing thickness (the direct to indirect band gap transition from mono- to bi-layer flakes[24, 25, 26]). Similarly, the thickness dependent band structure of WSe_2 flakes was investigated and we observed the same evolution of the VBM valley position from K to Γ when the flake thickness increases from one to two layers (Fig. 6); the band structure of bi-layer and multi-layer flakes also show general similarity. Interestingly, in WSe_2, the energy difference of the valence band between K and Γ is ~100 meV [Fig. 6c(iii)], which is 5 times smaller than that of MoS_2 [Fig. 5c(iii)]. Such significant difference implies that the hole spin may be more robust in bilayer WSe_2 than MoS_2, making it a promising system for bilayer based spin and valley device applications[21].

With the systematic study of the electronic structure of three representative MX_2 compounds and their valley locus evolution with thickness down to the mono-layer limit, we establish a solid basis to understand the underlying physics of these materials. This work further provides important guidance for new materials design and novel valleytronics device development, and also demonstrates the power of the *in situ* study of the band structure of sub-micron size semiconductors used in functional devices.

All PES experiments were performed in ultrahigh vacuum chambers under a base pressure better than 5×10^{-10} Torr. High-resolution ARPES experiments for bulk samples were performed at beamline 10.0.1 at the Advanced Light Source, using incident photon energies from 35 to 75 eV with energy resolution of 15 meV and angular resolution of 0.2°. The samples were cleaved *in situ* and kept at 20 K during the ARPES measurements. Spatially resolved ARPES data were obtained at the Spectromicroscopy beamline at the Elettra Synchrotron Light Laboratory, using photon energies 74 eV, with energy and angle resolutions of 50 meV and 0.2°, respectively. The spatial resolution was 800 nm, and the sample was maintained at 100 K during the measurements. After loading the sample into the ultrahigh vacuum chamber for ARPES measurement, an annealing process at 400ºC for 20 minutes was performed to clean the sample surface.

To experimentally access a full map of the MX_2 band structure in the mono-layer limit, in addition to the technical difficulty of the large beam size in normal ARPES (typically hundreds of micrometers) for measuring small samples, the very low conductivity of mono-layer MX_2 and the resulting charging effects impose serious technical difficulties. In this study, after a 2H-MoS_2 single crystal was exfoliated into flakes with varying thicknesses, we transferred them onto a CVD-graphene covered SiO_2/Si wafer. The graphene layer not only mechanically supports but also electrically grounds the MoS_2 flakes, and thus greatly suppresses the charging effect in the MoS_2 ultrathin flakes. The combination of the application of a conducting graphene-covered wafer and the implementation of spatially-resolved ARPES, as schematically shown in Fig. 4a and b, enables us to measure ultrathin MoS_2 samples with high spatial resolution. Micro-Raman spectroscopy was performed under ambient conditions with pump radiation operating at a wavelength of 532 nm and with the Si Raman band at 520 cm^{-1} as the reference. The Raman emission was collected by a 100× objective in a backscattering geometry and with instrumental spectral resolution of 1.0 cm^{-1}. To perform micro-photoluminescence, the excitation laser was at normal incidence on the sample at room temperature, with a spot size of 2 μm. The laser intensity was 100 W/cm^2 at a wavelength of 532 nm.

Electronic structure calculations were performed within the context of density functional theory

using the Projector augmented wave pseudopotentials method with plane wave basis as implemented in the VASP code. The exchange-correlation functional was treated using the Perdew-Burke-Ernzerhof generalized-gradient approximation.[35] The kinetic energy cutoff was fixed to 400 eV. A 24×24×6 *k*-mesh was used for the self-consistent calculation, and spin-orbit coupling was taken into account. The lattice constant and internal atomic positions were fully relaxed with the force cutoff energy of 0.01eV/Å.

Acknowledgements

Y.L.C. and B.Z. acknowledge support from the EPSRC (UK) grant EP/K04074X/1 and a DARPA (US) MESO project (no. N66001-11-1-4105). H.T.Y., Z.K.L., G.X., Z.H., S.C.Z., Z.X.S., H.Y.H. and Y.C. acknowledge support from the Department of Energy, Office of Basic Energy Sciences, Division of Materials Sciences and Engineering, under contract DE-AC02-76SF00515. S.W. and X.X. are supported by DoE, BES, Division of Materials Sciences and Engineering (DE-SC0008145).

Author Contribution

H.T.Y. Z.K.L. and G.X. equally contributed. H.T.Y. and Y.L.C. conceived and designed experiments. Y.L.C., H.T.Y., B.Z., Y.Z., V.K., M.Y. and A.B. performed ARPES measurements. G.X. and S.C.Z. performed all DFT calculations. H.T.Y. S.W. and K.Y. fabricated devices. S.W. and X.X. operated optical measurements. D.D. and Y.S.H. grew MX_2 crystals. Z.X.S., S.C.Z., Y.C. H.Y.H. and X.D.X. led experiments and discussions. H.T.Y. and Y.L.C. wrote the manuscript, with input from all authors.

Author Information The authors declare no competing financial interests. Correspondence and requests for materials should be addressed to Y.L.C., H.Y.H. and Y.C. (Yulin.Chen@physics.ox.ac.uk, hyhwang@stanford.edu, yicui@stanford.edu,).

References

1. Geim, A. K., Grigorieva, I. V. Van der Waals heterostructures. *Nature* 2013, **499**(7459)**:** 419-425.

2. Wang, Q. H., Kalantar-Zadeh, K., Kis, A., Coleman, J. N., Strano, M. S. Electronics and optoelectronics of two-dimensional transition metal dichalcogenides. *Nature Nanotechnol.* 2012, **7**(11)**:** 699-712.

3. Radisavljevic, B., Radenovic, A., Brivio, J., Giacometti, V., Kis, A. Single-layer MoS_2 transistors. *Nature Nanotechnol.* 2011, **6**(3)**:** 147-150.

4. Zeng, H. L., Dai, J. F., Yao, W., Xiao, D., Cui, X. D. Valley polarization in MoS_2 monolayers by optical pumping. *Nature Nanotechnol.* 2012, **7**(8)**:** 490-493.

5. Mak, K. F., He, K. L., Shan, J., Heinz, T. F. Control of valley polarization in monolayer MoS_2 by optical helicity. *Nature Nanotechnol.* 2012, **7**(8)**:** 494-498.

6. Cao, T., Wang, G., Han, W. P., Ye, H. Q., Zhu, C. R., Shi, J. R.*, et al.* Valley-selective circular dichroism of monolayer molybdenum disulphide. *Nature Commun.* 2012, **3:** 887.

7. Mak, K. F., He, K. L., Lee, C., Lee, G. H., Hone, J., Heinz, T. F.*, et al.* Tightly bound trions in monolayer MoS_2. *Nature Mate.r* 2013, **12**(3)**:** 207-211.

8. Yuan, H. T., Bahramy, M. S., Morimoto, K., Wu, S. F., Nomura, K., Yang, B. J.*, et al.* Zeeman-type spin splitting controlled by an electric field. *Nature Phys.* 2013, **9**(9)**:** 563-569.

9. Chhowalla, M., Shin, H. S., Eda, G., Li, L. J., Loh, K. P., Zhang, H. The chemistry of two-dimensional layered transition metal dichalcogenide nanosheets. *Nature Chem.* 2013, **5**(4)**:** 263-275.

10. Kibsgaard, J., Chen, Z. B., Reinecke, B. N., Jaramillo, T. F. Engineering the surface structure of MoS_2 to preferentially expose active edge sites for electrocatalysis. *Nature Mater.* 2012, **11**(11)**:** 963-969.

11. Voiry, D., Yamaguchi, H., Li, J. W., Silva, R., Alves, D. C. B., Fujita, T.*, et al.* Enhanced catalytic activity in strained chemically exfoliated WS_2 nanosheets for hydrogen evolution. *Nature Mater.* 2013, **12**(9)**:** 850-855.

12. Xiao, D., Liu, G. B., Feng, W. X., Xu, X. D., Yao, W. Coupled spin and valley physics in monolayers of MoS_2 and other group-VI dichalcogenides. *Phys. Rev. Lett.* 2012, **108**(19) 196802.

13. Shan, W. Y., Lu, H. Z., Xiao, D. Spin Hall effect in spin-valley coupled monolayers of transition metal dichalcogenides. *Phys. Rev. B* 2013, **88**(12) 125301.

14. Yao, W., Xiao, D., Niu Q. Valley-dependent optoelectronics from inversion symmetry breaking. *Phys. Rev. B* 2008, **77**(23) 235406.

15. Rycerz, A., Tworzydlo, J., Beenakker, C. W. J. Valley filter and valley valve in graphene. *Nature Phys.* 2007, **3**(3)**:** 172-175.

16. Zhu, Z. Y., Cheng, Y. C., Schwingenschlogl, U. Giant spin-orbit-induced spin splitting in two-dimensional transition-metal dichalcogenide semiconductors. *Phys. Rev. B* 2011, **84**(15) 153402.

17. Li, X., Zhang, F., Niu, Q. Unconventional Quantum Hall effect and tunable spin Hall effect in Dirac materials: application to an isolated MoS_2 trilayer. *Phys. Rev. Lett.* 2013, **110**(6) 066803.

18. Cheng, Y. C., Zhu, Z. Y., Tahir, M., Schwingenschlogl, U. Spin-orbit-induced spin splittings in polar transition metal dichalcogenide monolayers. *E.P.L.* 2013, **102**(5) 57001.

19 Lu, H. Z., Yao, W., Xiao, D., Shen, S. Q. Intervalley scattering and localization behaviors of spin-valley coupled dirac Fermions. *Phys. Rev. Lett.* 2013, **110**(1) 016806.

20. Ross, J. S., Wu, S. F., Yu, H. Y., Ghimire, N. J., Jones, A. M., Aivazian, G*., et al.* Electrical control of neutral and charged excitons in a monolayer semiconductor. *Nature Commun.* 2013, **4** 1474.

21. Wu, S. F., Ross, J. S., Liu, G. B., Aivazian, G., Jones, A., Fei, Z. Y*., et al.* Electrical tuning of valley magnetic moment through symmetry control in bilayer MoS_2. *Nature Phys.* 2013, **9**(3)**:** 149-153.

22. Mak, K. F., Lee, C., Hone, J., Shan, J., Heinz, T. F. Atomically thin MoS_2: A new direct-gap semiconductor. *Phys. Rev. Lett.* 2010, **105**(13) 136805.

23. Splendiani, A., Sun, L., Zhang, Y. B., Li, T. S., Kim, J., Chim, C. Y*., et al.* Emerging photoluminescence in monolayer MoS_2. *Nano Lett.* 2010, **10**(4)**:** 1271-1275.

24. Cheiwchanchamnangij, T., Lambrecht, W. R. L. Quasiparticle band structure calculation of monolayer, bilayer, and bulk MoS_2. *Phys. Rev. B* 2012, **85**(20) 205302.

25. Han, S.W., Kwon, H., Kim, S. K., Ryu, S., Yun, W. S., Kim, D. H*., et al.* Band-gap transition induced by interlayer van der Waals interaction in MoS_2. *Phys. Rev. B* 2011, **84**(4) 045409.

26. Jin, W. C., Yeh, P. C., Zaki, N., Zhang, D. T., Sadowski, J. T., Al-Mahboob, A*., et al.* Direct measurement of the

thickness-dependent electronic band structure of MoS_2 using angle-resolved photoemission spectroscopy. *Phys. Rev. Lett.* 2013, **111**(10) 106801.

27. Zhang, Y., Chang, T. R., Zhou, B., Cui, Y. T., Yan, H., Liu, Z. K.*, et al.* Direct observation of the transition from indirect to direct bandgap in atomically thin epitaxial $MoSe_2$. *Nature Nanotechnol.* 2014, **9**(2)**:** 111-115.

28. Gong, Z., Liu, G. B., Yu, H., Xiao, D., Cui, X., Xu, X.*, et al.* Magnetoelectric effects and valley-controlled spin quantum gates in transition metal dichalcogenide bilayers. *Nature Commun.* 2013, **4:** 2053.

29. Novoselov, K. S., Geim, A. K., Morozov, S. V., Jiang, D., Katsnelson, M. I., Grigorieva, I. V.*, et al.* Two-dimensional gas of massless Dirac fermions in graphene. *Nature* 2005, **438**(7065)**:** 197-200.

30. Meyer, J. C., Geim, A. K., Katsnelson, M. I., Novoselov, K. S., Booth, T. J., Roth, S. The structure of suspended graphene sheets. *Nature* 2007, **446**(7131)**:** 60-63.

31. Novoselov, K. S., Jiang, Z., Zhang, Y., Morozov, S. V., Stormer, H. L., Zeitler, U.*, et al.* Room-temperature quantum hall effect in graphene. *Science* 2007, **315**(5817)**:** 1379-1379.

32. Novoselov, K. S., Geim, A. K., Morozov, S. V., Jiang, D., Zhang, Y., Dubonos, S. V.*, et al.* Electric field effect in atomically thin carbon films. *Science* 2004, **306**(5696)**:** 666-669.

33. Zhang, Y. B., Tan, Y. W., Stormer, H. L., Kim, P. Experimental observation of the quantum Hall effect and Berry's phase in graphene. *Nature* 2005, **438**(7065)**:** 201-204.

34. Lee, C., Yan, H., Brus, L. E., Heinz, T. F., Hone, J., Ryu, S. Anomalous Lattice Vibrations of Single- and Few-Layer MoS_2. *Acs Nano* 2010, **4**(5)**:** 2695-2700.

35. Perdew, J. P., Burke, K., Ernzerhof, M. Generalized gradient approximation made simple. *Phys. Rev. Lett.* 1996, **77**(18)**:** 3865-3868.

Figure 1 Crystal and electronic structure of layered 2H-MoS_2

a, Layered crystal structure of 2H-MX_2, where red balls represent M (Mo or W) atoms and blue balls represent X (S, Se, or Te) atoms. The in-plane lattice parameter (*a*) and the distance between the M and X layers (*d*) are indicated, which have a direct influence on the band structure. **b.** Schematic of the 3D Brillouin zone (BZ) of MX_2 and its projection onto the surface Brillouin zone, where high symmetry points are labeled. **c**, 3D illustration of the band structure of bulk MoS_2 obtained by ARPES measurements. A clear band splitting at K is observed. **d,** and **e,** 2D and 3D constant energy plots at different energy levels (the energy level of the VBM at Γ is defined as 0) show the evolution of band dispersion. **f,** The band structure of bulk MoS_2 measured after *K*-dosage. Evidently the CBM sits at the K point while the VBM is at Γ, showing an indirect band gap (1.4 eV as indicated) for the bulk MoS_2. **g,** Constant energy contours at the CBM and VBM (appearing at the corners and the center of the BZ), respectively.

Figure 2 Band structure of as-cleaved and *K*-dosed bulk MX_2 crystals

a, Band dispersion along the Γ-K direction of as-cleaved bulk MoS_2, WS_2 and WSe_2 in panel (i), (ii), and (iii), respectively. The band splitting and the energy difference between the apexes of the valence band at Γ and K are indicated. **b.** Band dispersions measured after *K*-dosing. **c.** Zoomed-in view of the band dispersion expanded from the regions marked in **b**, the intensity in panel (ii) and (iii) were enhanced by a factor of 10 to allow better visibility of the conduction band. One can clearly see that the CBM of MoS_2 (i) is located at the K point, while the CBM of WSe_2 (iii) is located at Λ. For WS_2 (ii), the bottoms of the conduction band at K and Λ are nearly degenerate. **d**. Fermi-surface map of K-doped MoS_2 (i), WS_2 (ii) and WSe_2 (iii), also showing the CBM evolution from K in MoS_2 (i) to Λ in WSe_2 (iii).

Figure 3 Influence of lattice parameters on band valley loci in electronic structure of bulk MoS_2

a, Evolution of the calculated MoS_2 band structure as a function of the in-plane lattice constant *a*. (with all other parameters fixed to the fully-relaxed value) From left to right, *a* values are 3.11 Å, 3.15 Å, 3.19 Å (relaxed value), 3.23 Å, and 3.27 Å, respectively. The red line is the lowermost conduction band, and the blue line is the uppermost valence band. **b,** Similar to **a** but as a function of the out-of-plane lattice constant *d*. From left to right, *d* values are 1.524 Å, 1,544 Å, 1,564 Å (relaxed value), 1.584 Å, 1.604 Å, respectively. **c,** The variation of the energy difference between the two conduction sub-band valleys at K and Λ points ($\Delta E_{\Lambda K}^{CB} = E_{\Lambda}^{CB} - E_{K}^{CB}$, red line and dots)), and the energy difference between the two valence sub-band maxima at K and Γ points ($\Delta E_{\Gamma K}^{VB} = E_{\Gamma}^{VB} - E_{K}^{VB}$, blue line and dots), as a function of *a* and *d*, respectively. **d,** Phase diagram of $\Delta E_{\Lambda K}^{CB}$ as a function of *a* and *d*, in which $\Delta E_{\Lambda K}^{CB} < 0$ indicates that the conduction band at K is higher than Λ, while $\Delta E_{\Lambda K}^{CB} > 0$ indicates the opposite. Thicker black line indicates the boundary where $\Delta E_{\Lambda K}^{CB} = 0$; and the red "+" sign indicating the position of the calculated $\Delta E_{\Lambda K}^{CB}$ of MoS_2 with relaxed parameters.

Figure 4 Fabrication of ultrathin MoS_2 flakes via mechanical exfoliation and precise layer number identification

a, Schematic diagram of the spatially resolved ARPES setup. **b-d,** Optical (**b, c**) and AFM (**d**) images of exfoliated MoS_2 flakes with different magnification. A mono-layer flake is shown in **d** with an AFM depth profile scan showing the 0.7 nm thickness. **e,** Typical room temperature Raman spectra on MoS_2 flakes from bulk (black) to monolayer (red), which clearly exhibit sensitive thickness dependence. For a mono-layer, these Raman modes occur at 384 cm^{-1} and 403 cm^{-1}, with the energy difference of 19 cm^{-1} confirming the single layer form of MoS_2. Inset: the optical image of the flakes used, and the A, B, and C indication of the mono-, bi- and multi-layer regions measured. **f,** Comparison of room temperature photoluminescence (PL) on bulk and mono-layer MoS_2 and WSe_2 flakes. Green and purple are from mono-layer flakes; and black is from bulk WSe_2. Clearly, the strong PL is only observed in mono-layer flakes (with direct band gap).

Figure 5 Band valley evolution from multi-, bi- to mono-layer MoS_2 nano-flakes

a, 2D photoemission spectra intensity contrast map of MoS_2 flakes (measured at the Fermi level), with different magnifications from large area (i) to small area (iii), demonstrating the processes to locate the target mono-layer flake. Panel (iv) gives the optical image of the same flake, where the mono-, bi- and multi-layer MoS_2 flakes can be clearly seen. Points P1-P3 indicate the three measurement positions for mono-, bi- and multi-layer MoS_2 flakes. **b**, Constant energy plots measured at mono-layer (point P1), bilayer (point P2) and multilayer (point P3) spots, with the energy positions at E-E_{VBM} = 0 eV and E-E_{VBM} = - 0.5 eV, respectively. **c**, Band dispersions along the high symmetry K-Γ-K and M-Γ-M directions from point P1-P3, showing the band valley evolution with different flake thicknesses.

Figure 6 Band valley evolutions from multi-, bi- to mono-layer WSe_2 nano-flakes

a, 2D photoemission spectra intensity contrast map of WSe_2 flakes (measured at the Fermi level), with different magnifications from large area (i) to small area (iii), demonstrating the processes to locate the target mono-layer flake. Panel (iv) gives the optical image of the same flake, where the mono-, bi- and multi-layer WSe_2 flakes can be clearly seen. Points P1-P3 indicate the three measurement positions for mono-, bi- and multi-layer WSe_2 flakes. **b**, Constant energy plots measured at mono-layer (point P1), bilayer (point P2) and multilayer (point P3) spots, with the energy positions at E-E_{VBM} = 0 eV and E-E_{VBM} = - 0.5 eV, respectively. **c**, Band dispersions along the high symmetry K-Γ-K and M-Γ-M directions from point P1-P3, showing the band valley evolution with different flake thicknesses.

Figure 1

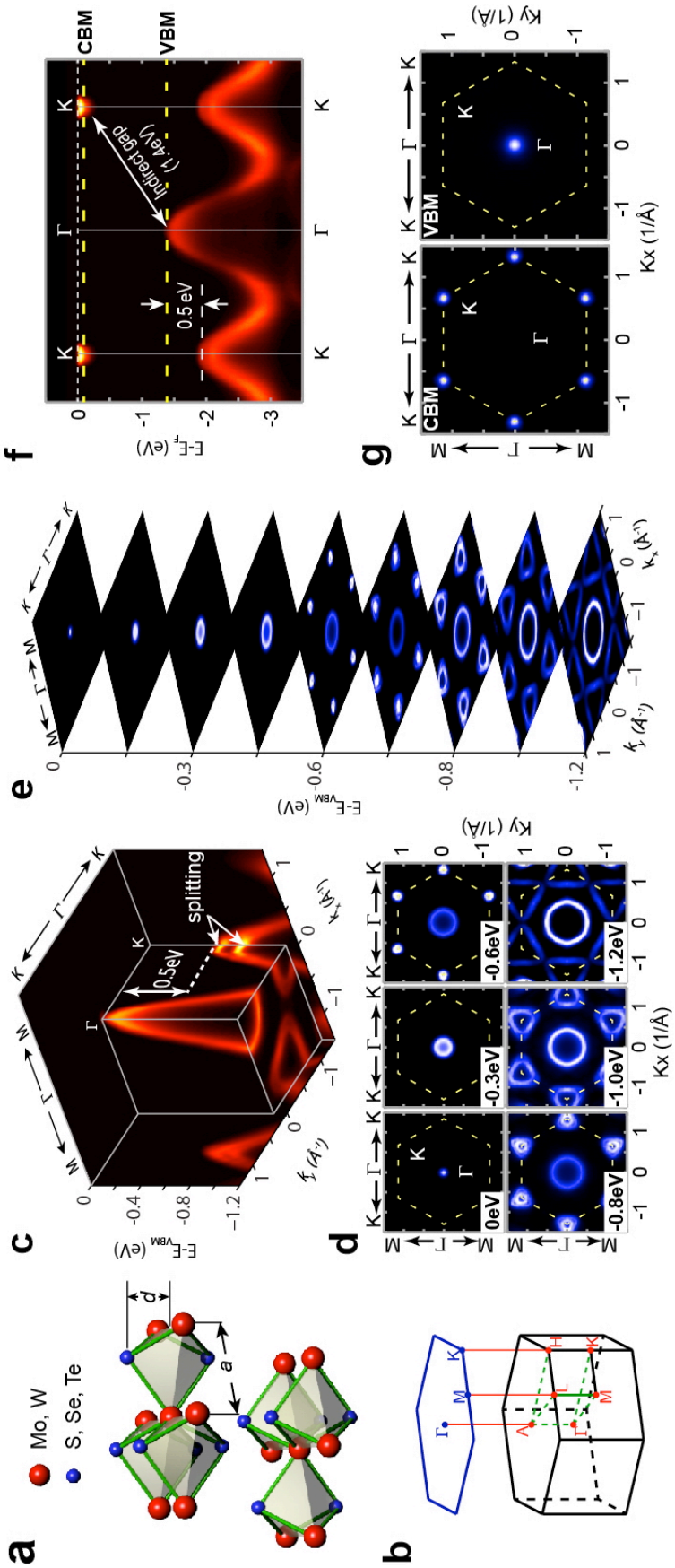
a
Mo, W
S, Se, Te
d
a
b
Γ
M
K
A
L
H
c
E-E_VBM (eV)
splitting
0.5eV
d
Ky (1/Å)
Kx (1/Å)
0eV
-0.3eV
-0.6eV
-0.8eV
-1.0eV
-1.2eV
e
E-E_VBM (eV)
f
E-E_F (eV)
CBM
VBM
0.5 eV
Indirect gap
(1.4eV)
g
CBM
VBM
Ky (1/Å)
Kx (1/Å)

Figure 2

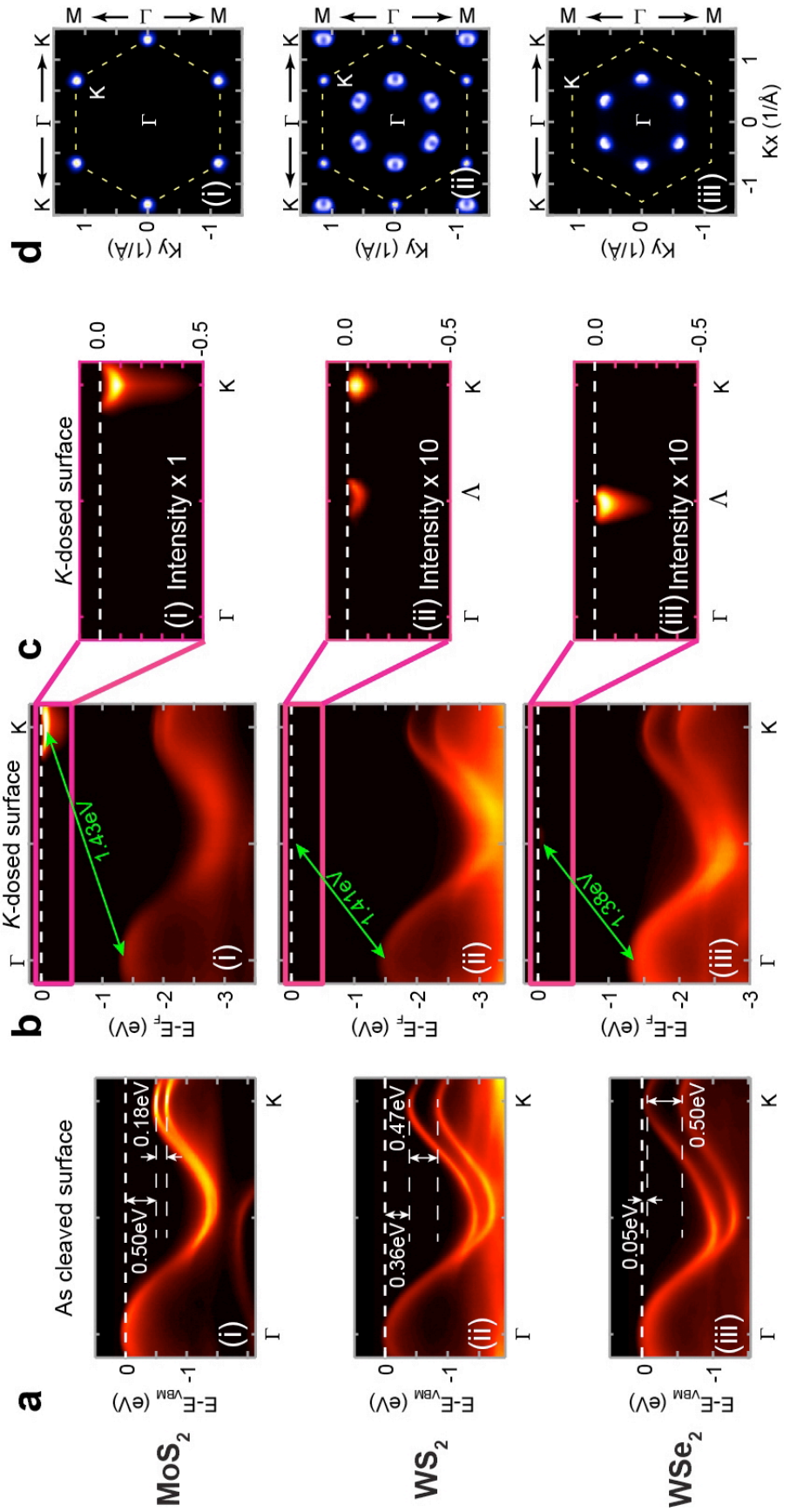
a
As cleaved surface
MoS2
WS2
WSe2
E-EVBM (eV)
0.50eV
0.18eV
0.36eV
0.47eV
0.05eV
0.50eV
(i)
(ii)
(iii)
Γ
K
b
K-dosed surface
E-EF (eV)
1.43eV
1.47eV
1.38eV
c
K-dosed surface
(i) Intensity x 1
(ii) Intensity x 10
(iii) Intensity x 10
Λ
d
Ky (1/Å)
Kx (1/Å)
M

Figure 3

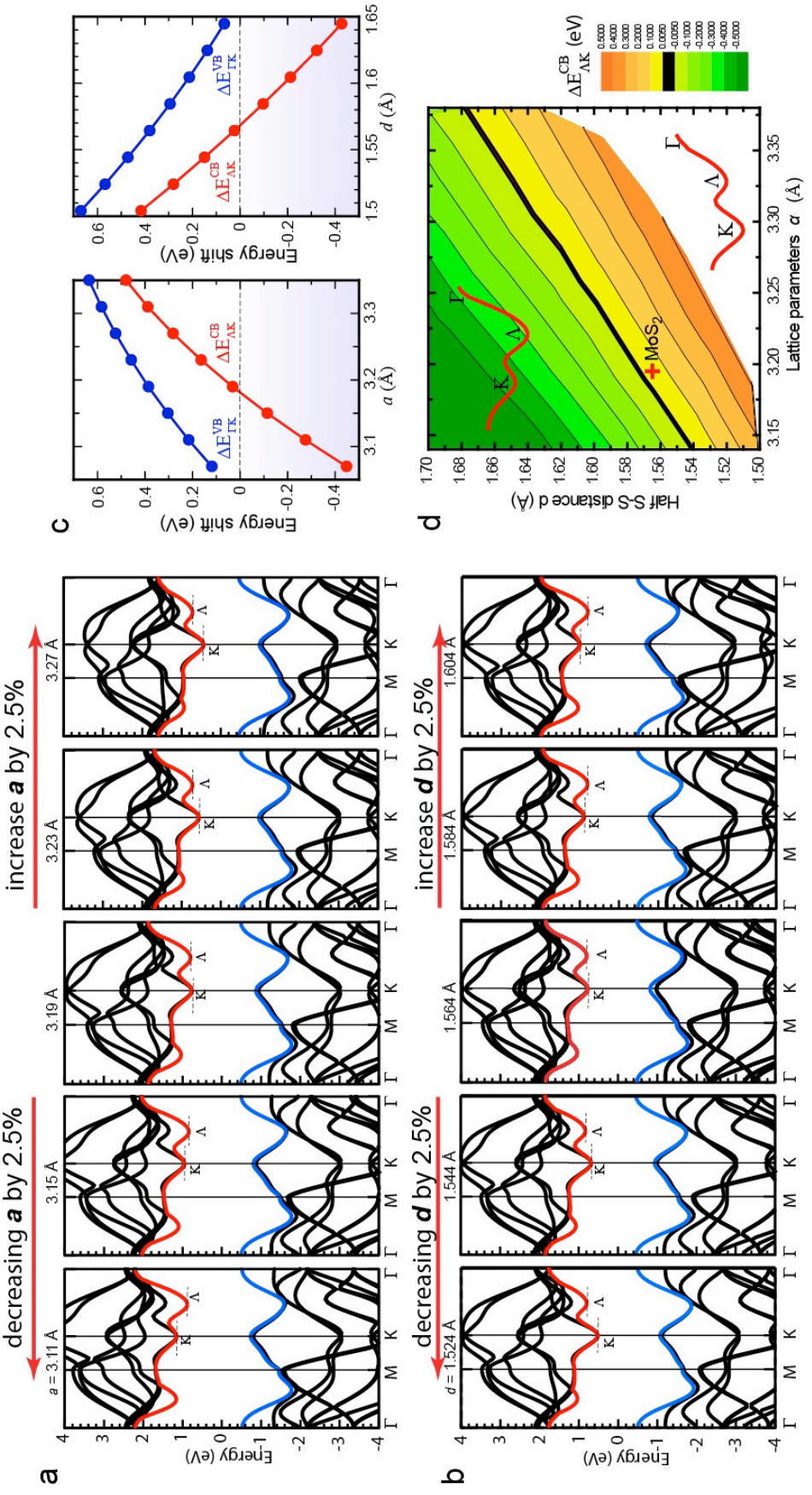
a
b
c
d
decreasing a by 2.5%
increase a by 2.5%
decreasing d by 2.5%
increase d by 2.5%
Energy (eV)
Energy shift (eV)
a (Å)
d (Å)
Half S-S distance d (Å)
Lattice parameters a (Å)
MoS2
Γ
K
Λ
M

Figure 4

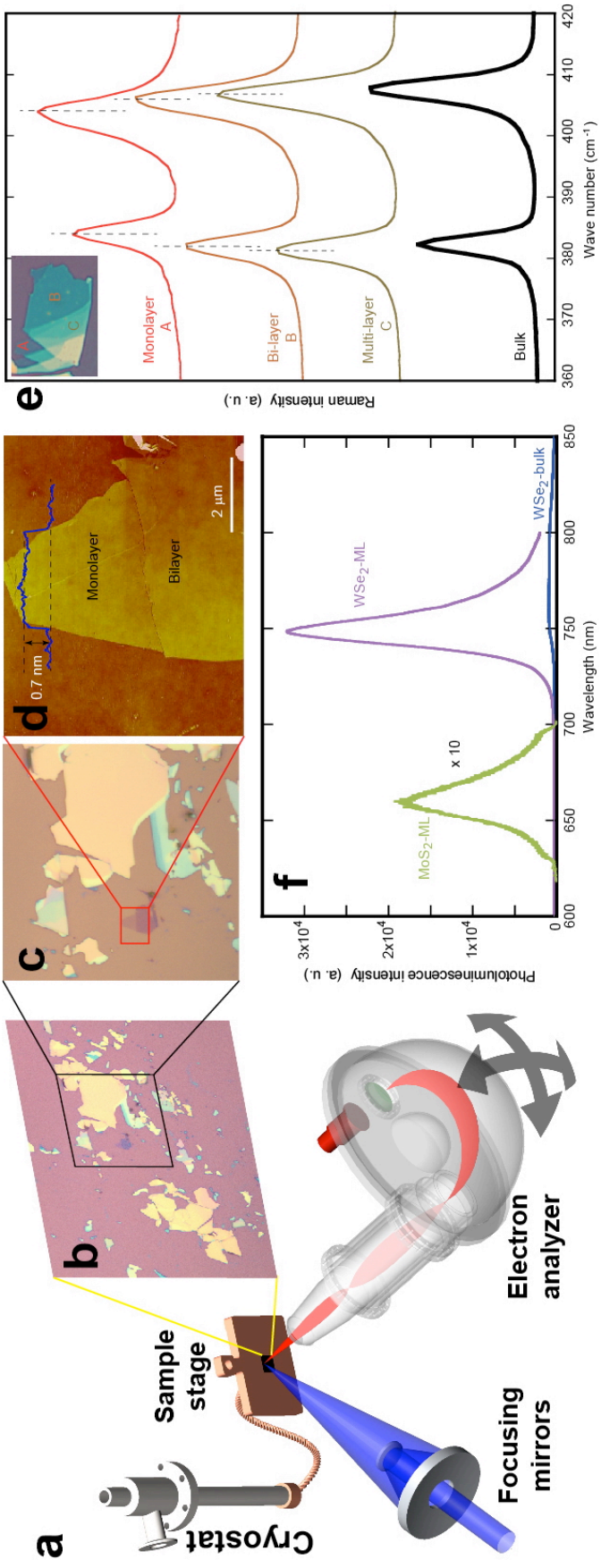
a
Cryostat
Sample stage
Focusing mirrors
Electron analyzer
b
c
d
0.7 nm
Monolayer
Bilayer
2 μm
e
Raman intensity (a. u.)
Monolayer A
Bi-layer B
Multi-layer C
Bulk
Wave number (cm-1)
f
Photoluminescence intensity (a. u.)
WSe2-ML
MoS2-ML
x 10
WSe2-bulk
Wavelength (nm)

Figure 5

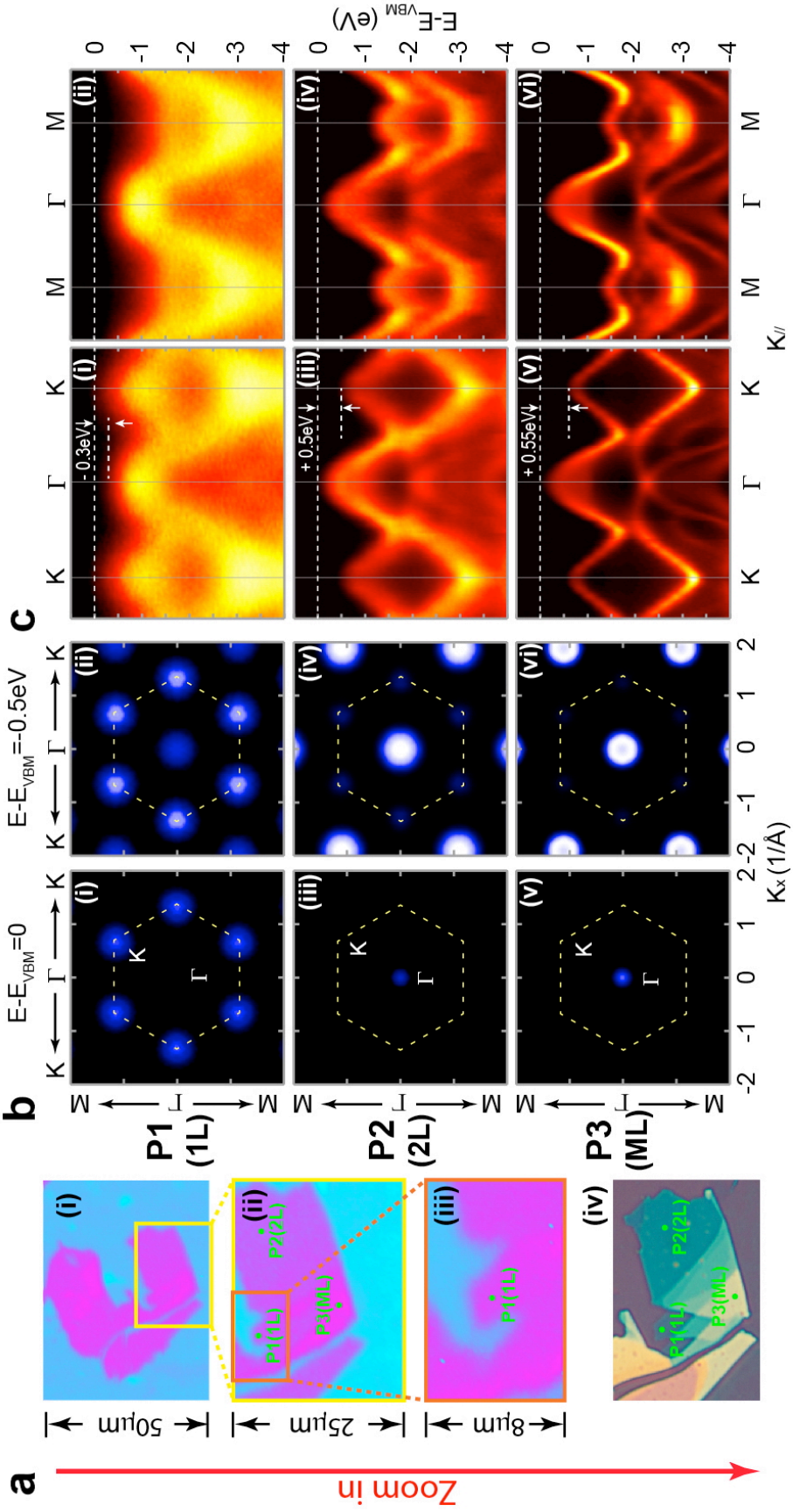
a
Zoom in
50μm
25μm
8μm
(i)
(ii)
(iii)
(iv)
P1(1L)
P2(2L)
P3(ML)
b
P1 (1L)
P2 (2L)
P3 (ML)
E-E_VBM=0
E-E_VBM=-0.5eV
K
Γ
M
(i)
(ii)
(iii)
(iv)
(v)
(vi)
Kx (1/Å)
c
- 0.3eV
+ 0.5eV
+ 0.55eV
E-E_VBM (eV)
K//

Figure 6

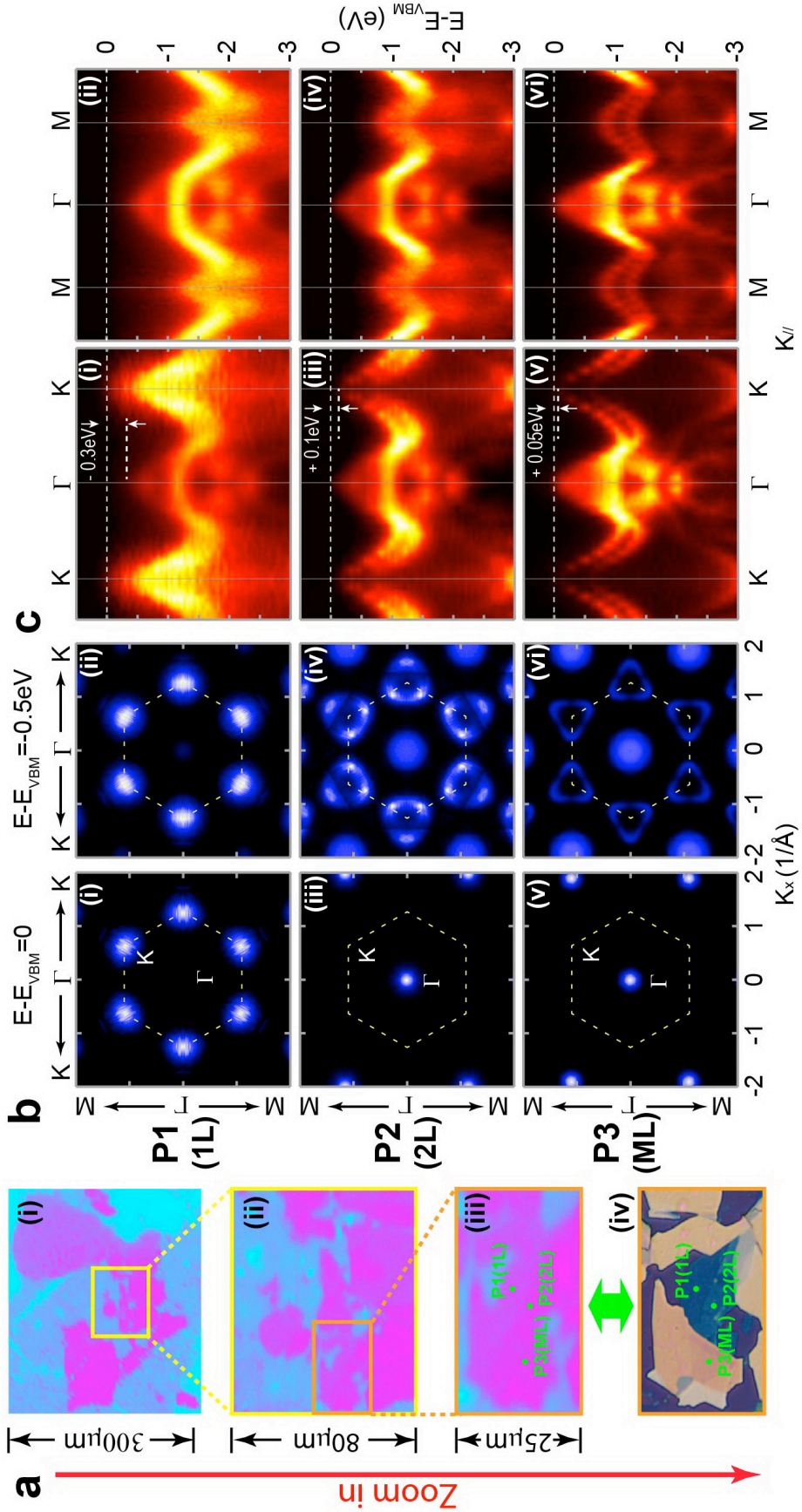
a
Zoom in
300μm
80μm
25μm
(i)
(ii)
(iii)
(iv)
P1(1L)
P2(2L)
P3(ML)
b
E-E_VBM=0
E-E_VBM=-0.5eV
P1 (1L)
P2 (2L)
P3 (ML)
K
Γ
M
c
- 0.3eV
+ 0.1eV
+ 0.05eV
E-E_VBM (eV)
K_x (1/Å)
K_//